Electrochemical nitrate reduction to high-value ammonia on two-dimensional molybdenum carbide nanosheets for nitrate-containing wastewater upcycling

Science of the Total Environment 878 (2023) 163145

Contents lists available at ScienceDirect

Science of the Total Environment

journal homepage: www.elsevier.com/locate/scitotenv

Electrochemical nitrate reduction to high-value ammonia on two-dimensional molybdenum carbide nanosheets for nitrate-containing wastewater upcycling

Donglin Zhu [a], Guoguang Li [a], Xu Yan [b], Chunxia Geng [d], Li Gao [c,*]

[a] School of the Environment, Nanjing University, Nanjing 210023, PR China
[b] Huizhou Innovation Research Institute of Next Generation Industrial Internet, Huizhou 516006, PR China
[c] Institute for Sustainable Industries and Liveable Cities, Victoria University, PO Box 14428, Melbourne, Victoria 8001, Australia
[d] Beijing Water Planning Institute, Beijing 100089, PR China

HIGHLIGHTS

- Mo_2C NSs catalyst is fabricated through a chemical reduction method.
- More active sites are exposed by reducing the dimensionality of Mo_2C.
- Mo_2C NSs catalyst exhibits a high activity for NH_3 electrosynthesis.
- In situ characterizations reveal the reaction pathway of NO_3^--to-NH_3.

GRAPHICAL ABSTRACT

Ultrathin Mo2C nanosheets boost electrochemical nitrate reduction to ammonia.

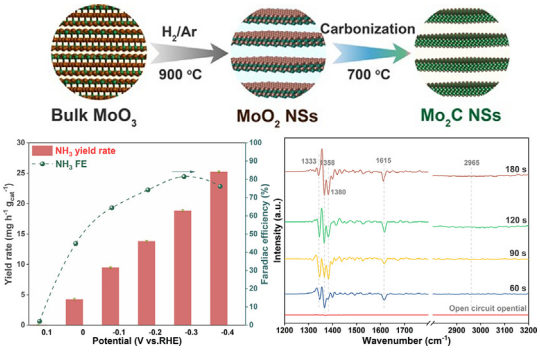

ARTICLE INFO

Editor: Qilin Wang

Keywords:
Nitrate wastewater upcycling
Electrochemical nitrate reduction
Ammonia electrosynthesis
Electrocatalysis
Molybdenum carbide

ABSTRACT

Electrochemical conversion of nitrate wastewater into high-value ammonia fertilizer has attracted extensive attention in wastewater treatment and resource recovery, but presents great challenges due to complicated reaction pathways and competing side reactions. Herein, we report a feasible method for the successful fabrication of Mo_2C nanosheets (Mo_2C NSs) as electrocatalyst for the electroreduction of nitrate to ammonia. Compared to Mo_2C nanoparticles, the Mo_2C NSs exhibited superior activity and selectivity in NH_3 electrosynthesis with an NH_3 yield rate of 25.2 $mg \cdot h^{-1} \cdot mg^{-1}_{cat.}$ at −0.4 V and a Faradaic efficiency of 81.4 % at −0.3 V versus reversible hydrogen electrode. The X-ray diffraction and transmission electron microscopy characterization verifted the controllable conversion of 2D MoO_2 NSs into 2D Mo_2C NSs. In situ spectroscopic studies and on-line differential electrochemical mass spectrometry revealed the proposed reaction pathway of NO_3^- to NH_3 conversion, $*NO_3^- \rightarrow *NO_2^- \rightarrow *NO \rightarrow *NOH \rightarrow *NH_2OH \rightarrow *NH_3$. Density functional theory calculations further verified the effective N-end NOH pathway with the conversion of $*NH_2OH$ to $*NH_2$ as the rate-determining step requiring a low energy barrier of 0.58 eV. Importantly, the key hydrogenation of *NO to form *NOH species underwent a lower energy barrier of 0.39 eV compared with the formation of *ONH species (1.06 eV).

* Corresponding author.
E-mail address: Li.gao@vu.edu.au (L. Gao).

http://dx.doi.org/10.1016/j.scitotenv.2023.163145
Received 15 February 2023; Received in revised form 24 March 2023; Accepted 25 March 2023
Available online 29 March 2023

1. Introduction

Nitrate accumulation in water environments from the heavy use of chemical fertilizers and the excessive discharge of industrial wastewater have posed a significant threat to the natural aquatic environments and human health (Li et al., 2022b; Xu et al., 2022a; Ding et al., 2023). In addition, nitrate is also a potential carcinogen because it is not fully reduced to produce nitrite, which can cause methemoglobinemia in infants and gastrointestinal cancer in adults (Picetti et al., 2022). The nitrogen in drinking water can also cause nitrogenous disinfection by-products (Yang et al., 2019; Xu et al., 2020). Hence, the nitrate concentration in drinking water can be limited to below 50 mg L^{-1} based on the recommendation of the World Health Organization (WHO) (Sun et al., 2022; Edition, 2011). Recently, various technologies, including adsorption, ion exchange, biological denitrification and electrochemistry, have been developed to remove nitrate pollutants (Ebrahimi and Roberts, 2016; Meghdadi, 2018; Zhang et al., 2022a; Fan et al., 2022b). Among these nitrate removal technologies, electrochemical nitrate reduction process possesses unique benefits with green electronic operation and no production of secondary pollution as well as easy integration with other water treatment technologies. In general, electrochemical reduction can selectively convert nitrate into nitrogen gas (N_2) or ammonia (NH_3) products (Gao et al., 2021; Xu et al., 2022b). Particularly, ammonia is more important as a raw material for the synthesis of fertilizers and pharmaceuticals. At the same time, ammonia is regarded as a renewable energy carrier due to its advantages of high energy density, carbon-free and cost-effective transportation (Gao et al., 2022; He et al., 2022b; Gao et al., 2020). Free ammonia can also be used to improve anaerobic digestion process (Wang et al., 2019; Liu et al., 2021; Zhang et al., 2021). Compared with the Haber-Bosch process for ammonia synthesis with intensive energy consumption and huge CO_2 emission, electrochemical nitrate reduction to high-value ammonia offers a "two birds, one stone" strategy for nitrate removal and ammonia generation to achieve the goal of wastewater treatment and resource recovery.

Two great advantages of NH_3 electrosynthesis from NO_3^- should be considered. Firstly, the deoxygenation reaction of NO_3^- requires a lower energy of 204 kJ mol^{-1} compared to the breakage of the N≡N bond (941 kJ mol^{-1}) (Wang et al., 2021; Yin et al., 2021). Secondly, nitrate electroreduction possesses high reactivity for ammonia electrosynthesis with a favorable thermodynamic potential ($NO_3^- + 6H_2O + 8e^- \rightarrow NH_3 + 9OH^-$, $E^0 = 0.69$ V versus reversible hydrogen electrode (RHE), pH = 14) (Wang et al., 2020a). In spite of these merits, the electrochemical nitrate reduction reaction (NORR) involves multistep electron-coupled proton transfer, thus lowering the overall reaction kinetic rate (Teng et al., 2022). In addition, complicated products of the NORR, possibly including NO_2, N_2, and N_2O, also raise major challenges for the highly selective synthesis of ammonia (Garcia-Segura et al., 2018; Xu et al., 2022b). Importantly, the hydrogen evolution reaction (HER, $2H_2O + 2e^- \rightarrow H_2 + OH^-$, $E^0 = 0$ V versus RHE, pH = 14) triggered under cathodic bias voltage severely suppresses the whole NO_3^- reduction, which is detrimental to NH_3 evolution (Zhao et al., 2021). Therefore, it is desirable to rationally design and develop high-performance electrocatalysts with high activity and selectivity for the electrochemical nitrate reduction to NH_3.

Recently, transition metal carbides with unoccupied d-orbitals and high electrical conductivity have presented superior catalytic reactions (Qin et al., 2021; Zhong et al., 2016). Among these transition metal carbides, Mo_2C has received extensive attention and research for catalyzing N_2 to produce NH_3 (Fan et al., 2022a; Ren et al., 2019). Besides, the agglomeration of Mo_2C during the synthesis process can give rise to low utilization efficiency of the catalytically active sites (Zhang et al., 2018). Notably, two-dimensional (2D) layered nanomaterials possess a large specific surface area and tunable crystal face, leading to the exposure of more active sites (Wang et al., 2020b). Hence, the controllable preparation of 2D molybdenum carbide catalyst would be an effective strategy for improving both the activity and selectivity of the NORR, which has not been reported yet.

Herein, we report a feasible and appealing strategy for the fabrication of Mo_2C nanosheets (Mo_2C NSs) by carbonizing the MoO_2 nanosheet template. The transformation of the crystal structure from MoO_2 NSs to Mo_2C NSs could be confirmed by X-ray diffraction and X-ray photoelectron spectroscopy. The synthesized Mo_2C NSs catalyst exhibited outstanding catalytic and selective activity toward the NORR in alkaline-nitrate aqueous electrolytes with an NH_3 yield rate of 25.2 $mg{\cdot}h^{-1}{\cdot}mg^{-1}_{cat.}$ at −0.4 V versus RHE and a faradaic efficiency of 81.4 % at −0.3 V versus RHE, as well as good durability. Operando electrochemical impedance spectroscopy suggested the more rapid charge transfer of the Mo_2C NSs at the electrode-electrolyte interface and the faster NORR kinetics compared with Mo_2C NPs. In situ spectroscopic analysis and on-line differential electrochemical mass spectrometry indicated the proposed NORR pathway, $*NO_3^- \rightarrow *NO_2^- \rightarrow *NO \rightarrow *NOH \rightarrow *NH_2OH \rightarrow *NH_3$. Theoretical calculations further showed that the lower energy barrier of the *NOH intermediate formed from *NO hydrogenation supported the above NORR pathway.

2. Experimental section

2.1. Synthesis of the Mo_2C nanosheets

2D MoO_2 nanosheets were obtained according to a previously reported method (Zhang et al., 2019). Typically, commercial MoO_3 powder placed into a quartz boat in a tubular furnace were sublimated at 900 °C for 60 min in a gas mixture (10%H_2/90%Ar, 100 sccm). After natural cooling, the MoO_2 nanosheets can be collected at the tail end of the quartz tube at room temperature. To prepare the Mo_2C NSs, the obtained MoO_2 NSs were mixed with 500 mg of commercial glucose powder, placed in a tube furnace and calcined at 700 °C for 2 h in Ar-H_2 gas. As a comparison, Mo_2C nanoparticles (Mo_2C NPs) were synthesized via the carbonization of MoO_2 powder under the same conditions.

2.2. Structural characterization

The phase compositions of the samples were determined by powder X-ray diffraction (XRD, Panalytical Inc., Netherlands) using Cu Kα radiation (λ = 0.15406 nm) with a fixed slit. The morphologies of the samples were characterized by a field emission scanning electron microscope (SEM, Hitachi, Japan) and a transmission electron microscope (TEM) equipped with an X-ray energy-dispersive spectrometer (EDS) (ARM200, JEOL, Japan) at an accelerating voltage of 200 kV. X-ray photoelectron spectroscopy (XPS) was conducted on a PHI5000 Versa Probe system (UIvac-Phi, Japan), and the C 1s peak at 284.8 eV was used as a reference for calibration.

2.3. Electrochemical activity evaluation

The electrochemical reaction was measured using a three-electrode electrochemical station (Gamry) in an H-type cell with a Nafion 117 membrane. The concentration of KCl in Ag/AgCl electrode was 3.5 M KCl and the cell volume was 60 mL. The working electrode was prepared by mixing 2 mg of catalyst, 10 μL of Nafion solution (5 wt%) and 90 μL of ethanol solution, and the mixtures were sonicated for 1 h to evenly disperse the catalysts in solution. After dropping 20 μL of the dispersion onto cleaned carbon paper (1 cm × 1 cm), the catalyst loading was calculated to be 0.4 mg cm^{-2}. During the nitrate reduction tests, all the potentials versus Ag/AgCl were converted into reversible hydrogen electrode (RHE) based on the following equation: $E_{RHE} = E_{Ag/AgCl} + 0.059 \times pH + 0.197$. Two different nitrate concentrations (1.0 M NaOH or 1.0 M NaOH + 0.1 M $NaNO_3$) were used for activity evaluation. A 50 mL electrolyte volume in two sections of a gas-tight H-cell separated by a proton-exchanged Nafion 117 membrane was adopted. Linear sweep voltammogram (LSV) curves were measured at a sweep rate of 5 mV s^{-1}. The geometric surface area could be adopted when reporting current densities. Chronoamperometry tests were carried out at various potentials for 1 h to determine the ammonia yield rates and Faradaic efficiencies. Specifically, the ammonia yield

rate was calculated according to the equation yield rate = (C_{prod} × V) / (t × m_{cat}), and the corresponding Faradaic efficiency (FE) was as follows: FE = (N × F × C_{prod} × V) / Q, where C_{prod} is the produced ammonia concentration, V is the electrolyte volume, t is the nitrate reduction reaction time, m_{cat} is the loading amount of the catalyst, N is the eight electron number for ammonia production, F represents the Faradaic constant (96,485C mol^{-1}), and Q is the total charge consumed in the nitrate reduction reaction. Eight consecutive cycling tests were conducted every 1 h at a constant potential of −0.3 V versus RHE in 1.0 M NaOH + 0.1 M $NaNO_3$ solution. Operando electrochemical impedance spectroscopy (EIS) was measured in an H-type cell, and the electrolytes were 1 M NaOH or 1 M NaOH + 0.1 M $NaNO_3$. All impedance measurements were performed from 0.5 to −0.2 V versus RHE. The frequency ranged between 10^5 Hz and 0.01 Hz with an AC amplitude of 5 mV.

2.4. Electrochemical in situ spectroscopic measurements

Electrochemical in situ Fourier transform infrared (FTIR) spectroscopy measurements were carried out with a Nicolet iN10MX FTIR spectrometer (Thermo Fisher Scientific) in a three-electrode electrochemical cell. The recorded spectrum was set to 64 scans at a resolution of 4 cm^{-1}. The Pt wire was used as the counter electrode, while the Ag/AgCl electrode served as the reference electrode. The Mo_2C catalysts were used as the working electrode. The electrolyte was 1 M NaOH + 0.1 M $NaNO_3$. The open-circuit potential was set to obtain a background spectrum. Then, in situ spectra were collected by chronoamperometry at −0.1 V versus RHE with a time interval of 20 s. The on-line differential electrochemical mass spectrometry (DEMS) measurement was run in a specially designed electrochemical cell with 1 M NaOH and 0.1 M NO_3^- as the electrolyte. Ar was used as the carrier gas and flowed into the electrolyte steadily before and during the DEMS operation. Chronoamperometry was carried out at −0.2 versus RHE. After the baseline was stable, the corresponding mass signals started to appear. The next cycle was started after the electrochemical test was ended, and the mass signal dropped to the baseline level.

2.5. Other experimental methods

The product quantification and identification, isotope labelling experiments and density functional theory calculations are shown in the Supporting Information.

3. Results and discussions

3.1. Electrocatalyst synthesis and characterization

The Mo_2C NSs were fabricated via a simple two-step process (Fig. 1). First, the solid-state MoO_3 powders could be sublimated at the high temperature of 900 °C and then the gaseous MoO_3 was reduced to MoO_2 by a gas mixture of Ar-H_2, followed by depositing onto the end of the tube wall layer-by-layer at room temperature. The commercial MoO_3 with orthorhombic structure presented the random particles with the size range from a few micrometers to tens of micrometers (Fig. S1). Second, the Mo_2C NSs were carbonized via the reaction of glucose with MoO_2 NSs at 700 °C. The structural morphology of the MoO_2 NSs and Mo_2C NSs was analyzed by transmission electron microscopy (TEM). As shown Fig. 2a, MoO_2 NSs exhibited the flat and intact surface, and the thin laminated structure was clearly observed. The high-resolution TEM (HRTEM) image of MoO_2 NSs revealed clear fringes with lattice spacing value of ~0.24 nm, corresponding to the (200) plane of MoO_2 (Fig. 2b). The selected area electron diffraction (SAED) pattern presented a set of diffraction points, verifying the monocrystal nature of the MoO_2 NSs (Fig. 2c). After carbonization, Mo_2C NSs still inherited the 2D ultrathin characteristics (Fig. 2d). Additionally, a set of diffraction spots with 6-fold symmetry from the SAED pattern clearly showed the single crystalline nature of the Mo_2C NSs (Fig. 2f). Importantly, the hexagonal crystalline structure of the Mo_2C NSs could be observed based on the SAED pattern (Fig. 2f). The bright lattice fringes displayed the high crystallization of the Mo_2C nanosheets (Fig. 2e). The HRTEM image clearly showed that the ordered lattice fringes with an interplanar spacing of 0.24 nm was ascribed to the (002) plane of Mo_2C (Fig. 2e). The elemental mapping analysis of Mo_2C NSs shown in Fig. 2i demonstrated a uniform distribution of Mo and C elements, suggesting the successful preparation of Mo_2C NSs. For comparison, Mo_2C NPs were also prepared by using glucose as the carbon source to carbonize MoO_2 powder at 700 °C. The TEM image shown in Fig. 2g indicated the morphologies of the Mo_2C NPs was highly aggregated. In addition, lattice spacing values of 0.26 and 0.24 nm found under HRTEM matched well with the (100) and (002) lattice planes of Mo_2C (Fig. 2h).

The structure of the obtained samples was characterized by X-ray diffraction (XRD). As shown in Fig. 3a, the diffraction peaks might correspond to the monoclinic symmetry crystal structure of MoO_2 (space group P21/c, a = 5.611 Å, b = 4.856 Å, c = 5.628 Å, PDF# 73-1249) (Fangkoch et al., 2020). The characteristic peaks at 26.2°, 32.0°, 37.2°, 41.8°, 49.7° and 53.6° were attributed to the (011), (101), (200), (210), (121) and (211) crystal facets of MoO_2 (Fig. 3a). After reaction with glucose, the main peaks of the hexagonal β-Mo_2C phase were detected from the XRD pattern, which was assigned to the (100), (002), (101), (102), (110), and (103) crystal facets (space group P63/mm, a = 3.012 Å, b = 3.012 Å, c = 4.735 Å, PDF# 35-0787) (Wan et al., 2017). Besides, the diffraction peaks of the Mo_2C NPs matched well with the hexagonal β-Mo_2C phase. X-ray photoelectron spectroscopy (XPS) measurements were conducted to investigate the surface electronic structure of the Mo_2C electrocatalysts. The high-resolution Mo 3d spectrum of the MoO_2 NSs indicated the peaks of Mo^{4+} at 229.6 eV for Mo $3d_{5/2}$ and 232.7 eV for Mo $3d_{3/2}$, while the Mo^{6+} species at 231.1 eV and 235.0 eV were caused by the oxidation of Mo^{4+} in air (Fig. 3b) (He et al., 2022a). After carbonization, the emerging peaks of Mo $3d_{5/2}$ and Mo $3d_{3/2}$d at 228.6 eV and 231.8 eV suggested the presence of Mo^{2+}, which was attributed to Mo_2C (Li et al., 2022a). Notably, Mo^{4+} and Mo^{6+} species were also detected on the surface of pure Mo_2C possibly due to air contact (Fig. 3b). For the C 1s spectrum, the peaks of the Mo—C bond were found at 284.6 eV, while the peaks of C—C and C—O bonds could be observed at 285.0 and 286.2 eV, respectively (Fig. 3c) (Li et al., 2019).

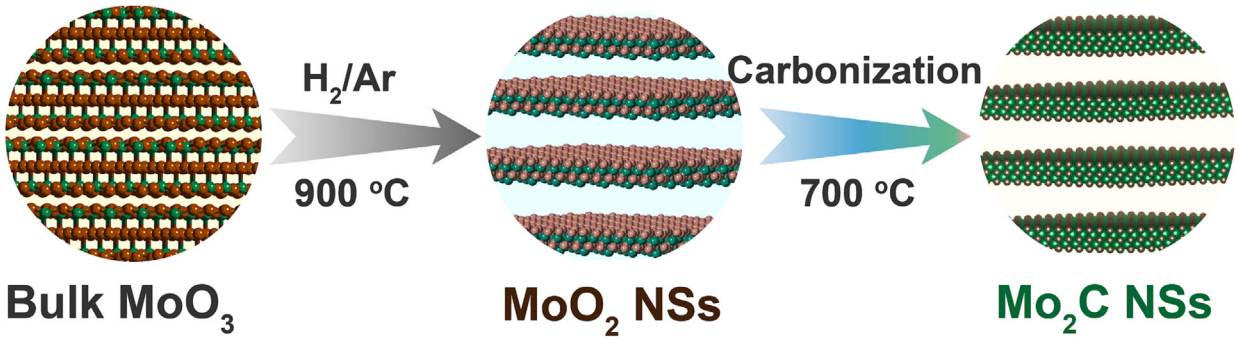

Fig. 1. Schematic illustration for the synthetic procedure of Mo_2C NSs.

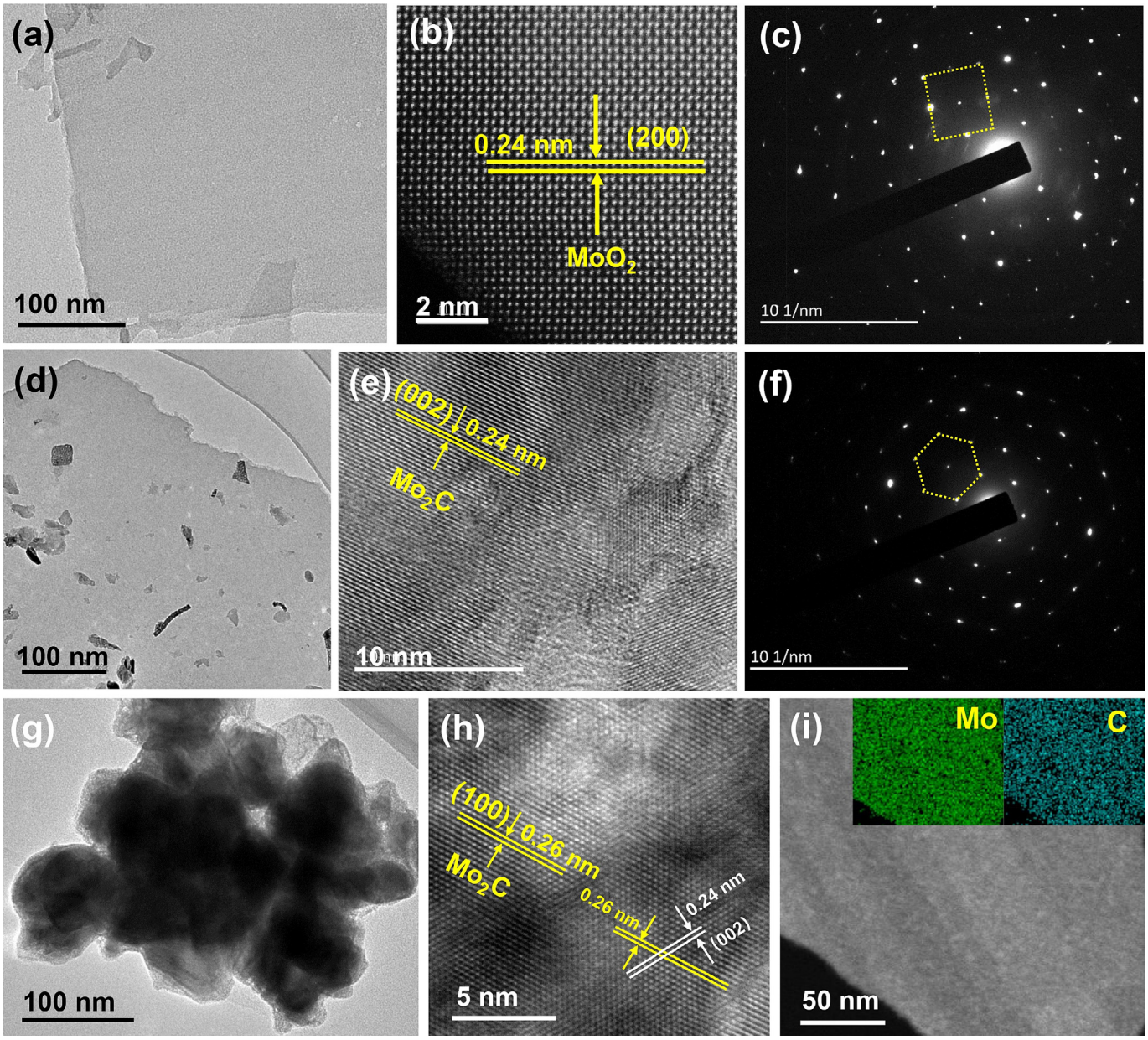

Fig. 2. (a) TEM and (b) HRTEM images of MoO_2 NSs. (c) the corresponding SAED images of MoO_2 NSs. (d) TEM and (e) HRTEM images of the Mo_2C NSs. (f) the SAED images of the Mo_2C NSs. (g) TEM and (h) HRTEM images of Mo_2C NPs. (i) EDS elemental mapping images of the Mo_2C NSs.

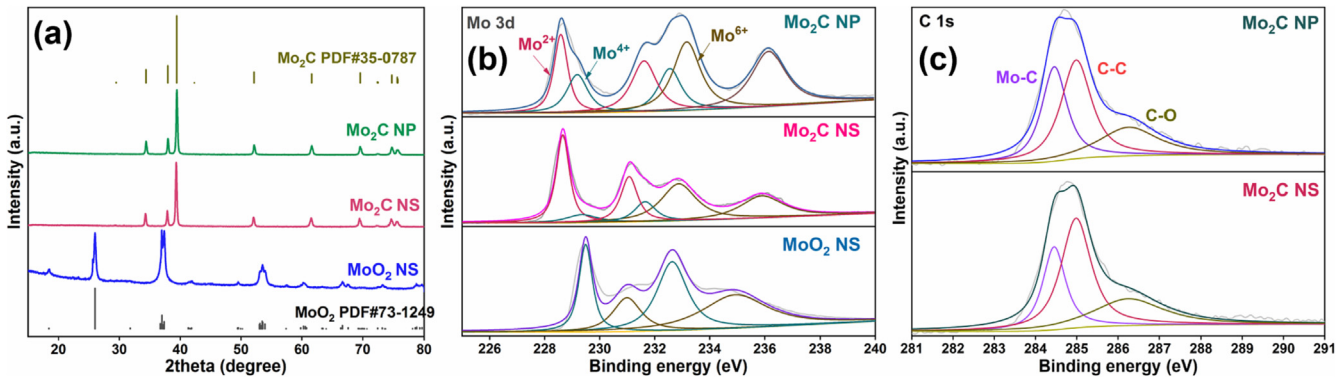

Fig. 3. (a) XRD pattern of Mo_2C NSs, Mo_2C NPs and MoO_2 NSs samples. High-resolution (b) Mo 3d and (c) C 1s XPS spectra of Mo_2C NSs and Mo_2C NPs samples.

3.2. Electrocatalytic performance for the NORR

The electrochemical activity of the Mo_2C electrocatalyst toward nitrate reduction was performed in a three-electrode system. The working electrode was a carbon paper containing catalyst powder. Linear sweep voltammetry (LSV) curves were recorded in a 1.0 M NaOH solution with or without 0.1 M NO_3^-. In the pure NaOH electrolyte, the Mo_2C NSs catalyst exhibited poor performance for low current response between 0.4 and −0.4 V versus RHE, indicating that Mo_2C catalyst could not effectively catalyze water reduction (Fig. 4a). The poor activity for H_2 evolution might be beneficial to chemisorption and activation of the proposed NO_3^-. However, after adding 0.1 M NO_3^-, the current density significantly increased, indicating the occurrence of substantial NO_3^- reduction (Fig. 4a). Notably, the Mo_2C NSs catalyst delivered enhanced activity for NO_3^- reduction with a higher current density compared with Mo_2C NPs under the same conditions (Fig. 4d). The LSV curves of the carbon paper showed the negligible current density for NO_3^- reduction (Fig. S2).

Subsequently, to identify and quantify the yield rate and Faradaic efficiency (FE) of produced NH_3 over the catalysts, chronoamperometric analysis was conducted at different working potentials. The amount of produced NH_3 at different potentials was measured via the indophenol blue reagent method using ultraviolet-visible (UV–Vis) spectrophotometry. Fig. 4b showed the time-resolved current density of Mo_2C NSs during an operation period of 1.0 h at a series of applied potentials from 0.1 to −0.4 V versus RHE. The current density was remarkably elevated when the applied potential became more negative. The NH_3 yield rate and the corresponding FE were plotted against the applied potentials (Fig. 4c). The NH_3 yield rate of the Mo_2C NSs gradually increased when the negative potential changed from 0.1 V to −0.4 V versus RHE (Fig. 4c). Correspondingly, a maximum NH_3 yield rate of 25.2 $mg{\cdot}h^{-1}{\cdot}mg^{-1}_{cat.}$ was detected at −0.4 V versus RHE. However, the NH_3 FE of Mo_2C NSs first increased with increasing potential and then began to decline when the potential exceeded −0.3 V versus RHE due to the competitive HER at higher overpotential. The highest FE value of produced NH_3 at −0.3 versus RHE was determined to be

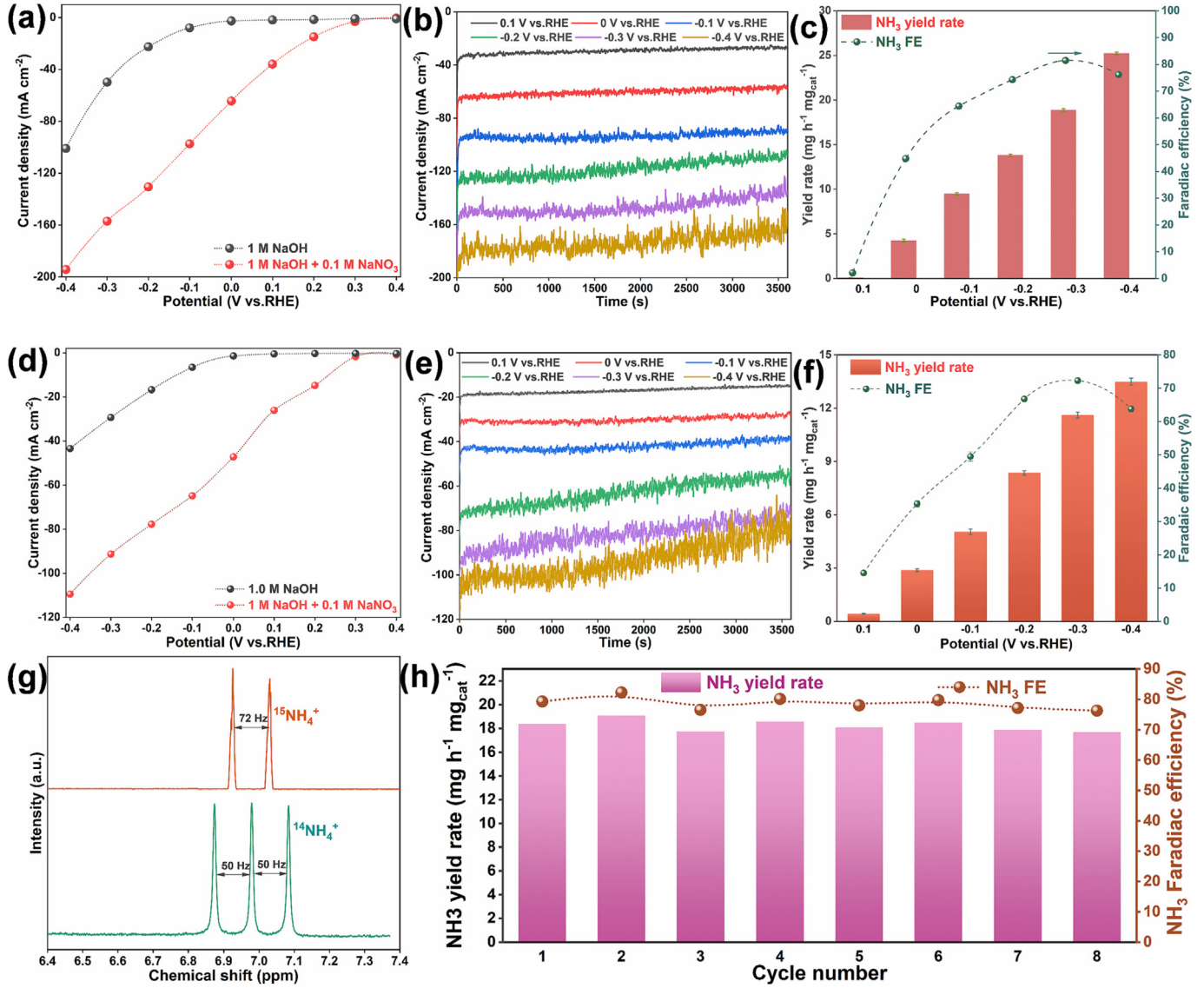

Fig. 4. LSV curves of (a) Mo_2C NSs and (d) the Mo_2C NPs in 1 M KOH electrolyte with and without 0.1 M nitrate. Chronoamperometric curves of (b) Mo_2C NSs and (e) the Mo_2C NPs at each given potential in 1 M KOH electrolyte with 0.1 M nitrate. Potential-dependent Faradaic efficiency (left axis) and NH_3 yield rates (right axis) of (c) Mo_2C NSs and (f) the Mo_2C NPs in 1 M KOH electrolyte with 0.1 M nitrate. (g) ^1H NMR spectra of generated $^{14}NH_4^+$ and $^{15}NH_4^+$ for the Ru NCs/MoO_2 NSs. (h) The cyclic stability test of the Mo_2C NSs.

81.4 %. The NORR performance of Mo_2C NSs was also comparable with the other materials (Table S1). Besides, the time-resolved current density of Mo_2C NPs was also presented in Fig. 4e. The NH_3 yield rate and FE of the Mo_2C NPs were also detected and calculated at various potentials, indicating the same trend as the Mo_2C NSs (Fig. 4f). The maximum NH_3 yield rate and FE of the Mo_2C NSs were determined to be 25.2 mg h^{-1} $mg^{-1}_{cat.}$ at −0.4 V versus RHE and 81.4 % at −0.3 V versus RHE, respectively, which were obviously lower than those of Mo_2C NPs (13.5 mg h^{-1} $mg^{-1}_{cat.}$ at −0.4 V versus RHE and 72.3 % at −0.3 V versus RHE, respectively). This suggests that the Mo_2C NSs could expose more active centers toward the nitrate reduction reaction compared with Mo_2C NPs. Besides, the effective electrochemically active surface area of the samples was estimated by measuring the double-layer capacitance (C_{dl}). The C_{dl} value increased from the 17.27 mF cm^{-2} of Mo_2C NPs to the 28.63 mF cm^{-2} of Mo_2C NSs, suggesting more accessible active sites exposed on Mo_2C NSs (Fig. S3).

To confirm the chemical origin of the NH_3 product from the supplied NO_3^- ions, an isotope labelling experiment using ^{15}N-labelled NO_3^- as the feedstock was carried out on Mo_2C NSs. The ^1H NMR spectra were featured by an obvious triplet with a coupling constant of 52 Hz, corresponding to $^{14}NH_4^+$ (Fig. 4g) (Wang et al., 2022). In addition, the ^{15}N nuclear spin produced a fine ^{15}N doublet at 72 Hz, which could be detected as the ^1H NMR signal of $^{15}NH_4^+$ in the region near 6.80–7.20 ppm, while no triple coupling of $^{14}NH_4^+$ could be detected (Fig. 4g) (Zheng et al., 2021). The isotope labelling tests confirmed that the ammonia products were generated by electrochemical nitrate reduction on Mo_2C NSs rather than other contaminations. Besides, the durability is also an important parameter to evaluate the catalysts. Consecutive cycling and chronoamperometry tests of Mo_2C NSs at −0.3 V versus RHE were carried out in alkaline-nitrate electrolyte. As shown in Fig. 4h, the yield rate and FE of ammonia products were well maintained over eight electrolysis cycles, demonstrating its strong robustness in electrochemical NORR. Several control experiments were also carried out to verify that the ammonia products were produced from the electrocatalytic NORR instead of the Mo_2C NSs themselves (Fig. S4). The open circuit potential (OCP) and pristine carbon paper without Mo_2C NSs were used as the operating conditions. No obvious NH_3 production was detected, revealing that Mo_2C NSs served as an active constituent in the constructed electrode.

3.3. Electrocatalytic reaction mechanism

Next, the electron transfer resistance and reaction kinetics of Mo_2C NSs during the nitrate reaction process were investigated by operando EIS. The Nyquist plots and Bode plots of five potentials obtained in 1.0 M NaOH with or without nitrate was also analyzed (Figs. 5 and S2). In the Nyquist plots of the pure NaOH system, the Nyquist spectra of Mo_2C NSs presented nearly oblique lines at low voltages from 0.1 to 0 V versus RHE, suggesting high resistance at the interface between the electrode and the electrolytes (Fig. 5a). As the applied voltage exceeded −0.1 V versus RHE, an obvious semicircle appeared, indicating the occurrence of the electrocatalytic HER. After introducing 0.1 M NO_3^-, the semicircle could be observed at lower voltage of −0.3 V versus RHE (Fig. 5c). Notably, the corresponding radius in the NO_3^- system was much smaller than that of the pure NaOH system, verifying that the electrocatalytic NORR appeared. In addition, the changes in the phase angle (θ_{peak}) and frequency were displayed in the Bode phase plots. In general, the phase angle peaks of the high-frequency region could be correlated with the electron conduction of the catalyst inner layer, while the phase angle peaks of the low-frequency area would correspond to the interface reaction charge transfer (Chen et al., 2022). As the potential was changed from 0.1 to −0.3 V versus RHE, the θ_{peak} amplitude in the pure NaOH system declined from 75 to 17, while the θ_{peak} in the alkaline-nitrate system changed from 62 to 13 (Fig. 5b and d). Notably, after 0.3 V versus RHE, the θ_{peak} of the nitrate-containing system was smaller than that of the pure NaOH system, implying a low resistance and high ion diffusion capacity. Besides, the Nyquist plots and Bode plots of Mo_2C NPs could be analyzed, indicating a similar trend to Mo_2C NSs in the NO_3^--containing or -free systems (Fig. S5). Further comparison of Bode plots in nitrate-containing solution demonstrated that the phase angles of Mo_2C NSs in the low-frequency region (approximately 0.01–10 Hz) were smaller than

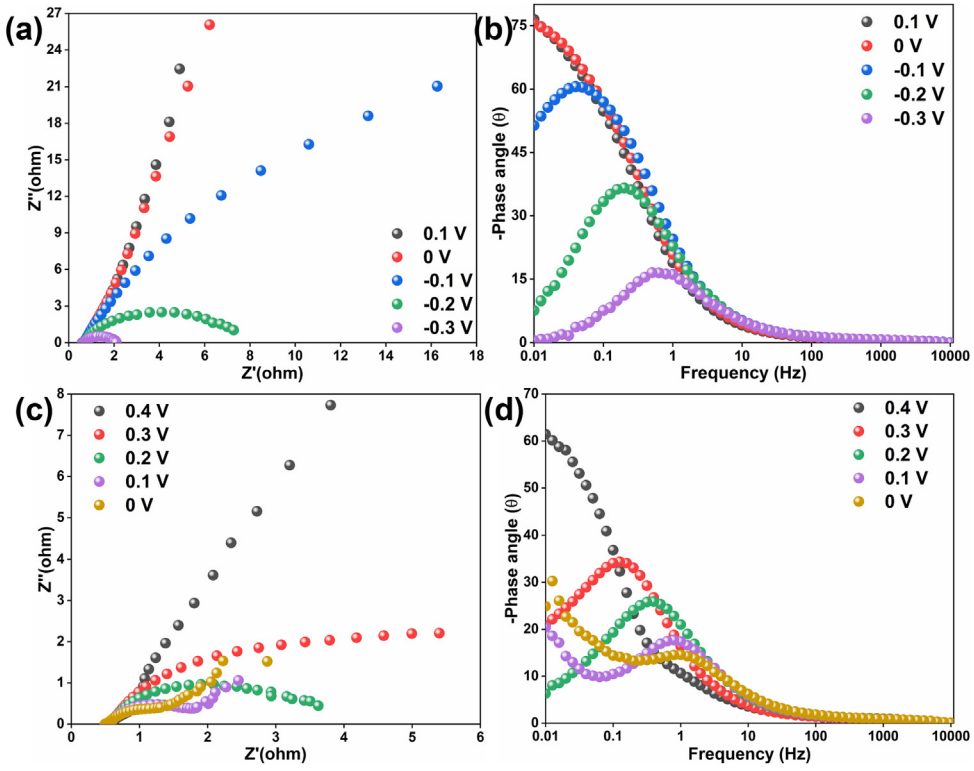

Fig. 5. Operando EIS analysis of the Mo_2C NSs electrode during the HER or NORR. (a) Nyquist plots and (b) Bode phase plots of the Mo_2C NSs during the HER. (c) Nyquist plots and (d) Bode phase plots of the Mo_2C NSs during the NORR.

those of Mo_2C NPs, suggesting rapid charge transfer at the electrode-electrolyte interface and faster NORR kinetics for Mo_2C NPs (Table S2).

The electrochemical nitrate reaction pathway on Mo_2C NSs was explored to understand the reaction mechanism. The intermediate nitrogen products generated by nitrate electroreduction were detected by on-line differential electrochemical mass spectrometry (DEMS). The mass-to-charge ratio (m/z) signals with varied time were displayed in Fig. 6a. It was clearly observed that the peak of m/z signals appeared periodically at 46, 30, 33 and 17, which were ascribed to NO_2, NO, NH_2OH and NH_3, respectively. But the peak of m/z signals at 44 assigned to N_2O was negligible and the byproduct N_2 was visible (Fig. S6). Subsequently, the possible nitrogen intermediates were investigated via electrochemical in situ Fourier transform infrared (FTIR) spectroscopy at a constant potential of −0.2 V (Fig. 6b). The negatively evolved band at 1380 cm^{-1} indicated that the nitrate species ($*NO_3^-$) were absorbed on the surface (Zhang et al., 2022b). The bands at 1333 cm^{-1} were assigned to the C_{2v} symmetry of NO_2^- while the bands at 1615 cm^{-1} corresponded to the monodentate coordination of *N-O species (Qin et al., 2022; Zhang et al., 2022b). The monitored NO_x species demonstrated the deoxygenation steps during NO_3^- reduction. In addition, a broad band at approximately 2965 cm^{-1} signified the related ν(N—H) stretching mode in NH_y species, and NH_2 wagging modes at 1358 cm^{-1} could be observed, indicating hydrogeneration for NH_3 evolution after deoxygenation (Gong et al., 2022; Kani et al., 2021). Based on the DEMS and in situ FTIR results, we proposed a nitrate reduction reaction pathway over Mo_2C NSs. The NORR could be broken down into a series of deoxygenation reactions, $*NO_3^- \rightarrow *NO_2^- \rightarrow *NO$, followed by hydrogenation steps $*NO \rightarrow *NOH \rightarrow *NH_2OH \rightarrow *NH_3$ and finally desorption of NH_3.

To further gain insight into the reaction pathway for the reduction of NO_3^- to NH_3, density functional theory (DFT) calculations were performed on the Mo_2C (002) model (Fig. 6c). After successive deoxygenation via the reaction of NO_3^- with two proton-electron pairs, the key *NO intermediate was produced with a free energy of −5.13 eV. Then, two different species (*NOH or *ONH) could be formed via the proton-electron pair attacking the O side or N side of *NO, respectively. This meant that hydrogenation pathways may occur in two cases, that is, the *N-end *NOH pathway ($*NO \rightarrow *NOH \rightarrow *NHOH \rightarrow *NH_2OH \rightarrow *NH_2 \rightarrow *NH_3$) and the O-end *ONH pathway ($*ON \rightarrow *ONH \rightarrow *ONH_2 \rightarrow *ONH_3 \rightarrow *OH \rightarrow *H_2O$). Apparently, for the O-end *ONH pathway, the $*ON \rightarrow *ONH$ step presented an endothermic reaction with a high energy barrier of 1.06 eV. In contrast, the *N-end NOH pathway underwent a low energy barrier of 0.39 eV for the endothermic step of $*NO \rightarrow *NOH$, suggesting that the *NOH species formed was more favorable than the *ONH species. Thereafter, the formation of *NHOH and $*NH_2OH$ species was exothermic with negative energies of −0.53 eV and −0.17 eV, respectively. An energy barrier of 0.58 eV was required to produce the $*NH_2$ intermediate, and then the $*NH_3$ intermediate was formed with a negative free energy change (−0.17 eV). In short, the rate-determining step (RDS) of the N-end NOH pathway was $*NH_2OH \rightarrow *NH_2$ with a free energy change of 0.58 eV, which was lower than that of the O-end *ONH pathway with the RDS of $*ON \rightarrow *ONH$ (1.06 eV).

4. Conclusion

In summary, we reported a feasible two-step approach for the preparation of ultrathin Mo_2C NSs via the carbonization of MoO_2 NSs using glucose as the carbon source. The Mo_2C NSs were considered an attractive catalyst for the electrochemical conversion of nitrate to NH_3. The HRTEM image clearly showed the single-crystal structure of Mo_2C NSs. In the alkaline-nitrate electrolyte, the catalyst achieved a maximum NH_3 yield of 25.2 mg h^{-1} mg_{cat}^{-1} at −0.4 V versus RHE and a maximum FE of 81.4 % at −0.3 V versus RHE. Besides, the catalyst presented high activity and stability after long-term electroreduction. In addition, operando EIS suggested that the Mo_2C NSs possessed rapid charge transfer at the electrode-electrolyte interface and faster NORR kinetics than the Mo_2C NPs. In situ FTIR and DEMS indicated the proposed nitrate reaction pathway, $*NO_3^- \rightarrow *NO_2^- \rightarrow *NO \rightarrow *NOH \rightarrow *NH_2OH \rightarrow *NH_3$. DFT calculations further verified the favorable pathway with a lower energy barrier of $*NO \rightarrow *NOH$ than that of the *ONH species formed. Our study not only provided an attractive electrocatalyst with excellent activity toward the NORR but also paved the way to optimize Mo-based electrocatalyst for electrocatalysis.

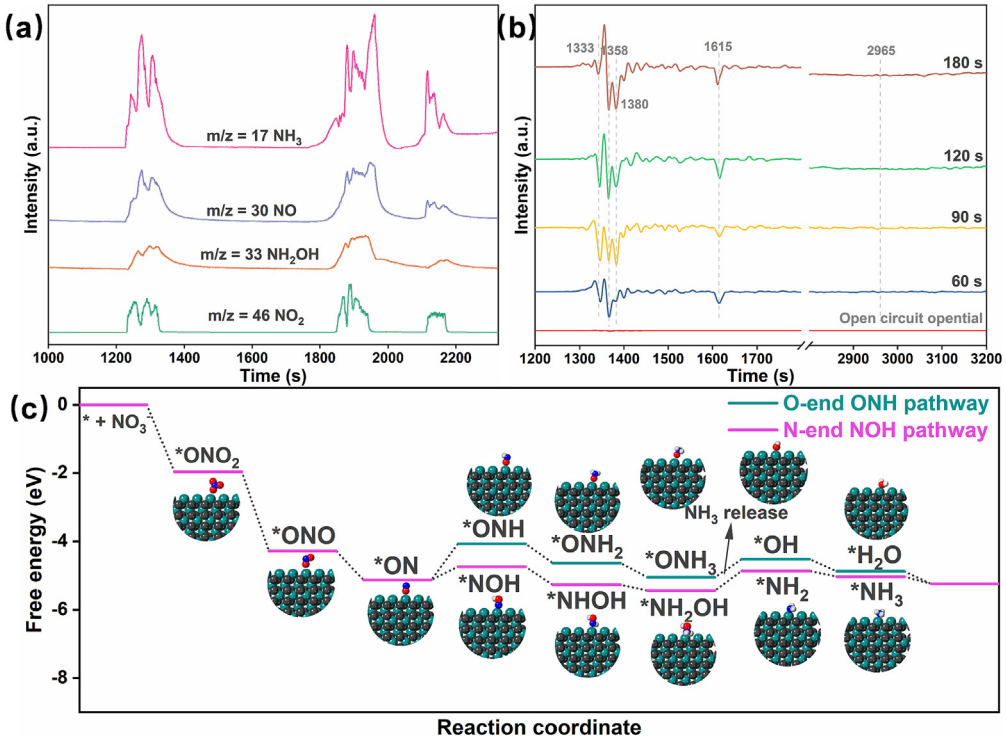

Fig. 6. (a) Online DEMS and (b) in situ FTIR spectra of the Mo_2C NSs during NORR. (c) Gibbs free-energy diagrams of reaction pathway for NO_3^- reduction to ammonia on the surface of the Mo_2C NSs.

CRediT authorship contribution statement

Donglin Zhu: Methodology, Data curation, Writing - Original draft preparation.
Guoguang Li: Conceptualization, Methodology, Software.
Xu Yan: Software, Validation.
Chunxia Geng: Writing - Reviewing and Editing.
Li Gao: Supervision.

Data availability

Data will be made available on request.

Declaration of competing interest

The authors declare that they have no known competing financial interests or personal relationships that could have appeared to influence the work reported in this paper.

Acknowledgement

This work was supported by the Key-Area Research and Development Program of Guangdong Province (2020B0101130001).

Appendix A. Supplementary data

Supplementary data to this article can be found online at https://doi.org/10.1016/j.scitotenv.2023.163145.

References

Chen, X., Wang, Q., Cheng, Y., Xing, H., Li, J., Zhu, X., et al., 2022. S-doping triggers redox reactivities of both iron and lattice oxygen in FeOOH for low-cost and high-performance water oxidation. Adv. Funct. Mater. 32, 2112674.
Ding, M., Xu, H., Yao, C., Chen, W., Song, N., Zhang, Q., Lin, T., Xie, Z., 2023. Understanding the membrane fouling control process at molecular level in the heated persulfate activation- membrane distillation hybrid system. Water Res. 229, 119465.
Ebrahimi, S., Roberts, D.J., 2016. Mathematical modelling and reactor design for multi-cycle bioregeneration of nitrate exhausted ion exchange resin. Water Res. 88, 766–776.
Edition, F., 2011. Guidelines for drinking-water quality. WHO Chron. 38, 398–399.
Fan, B., Wang, H., Zhang, H., Song, Y., Zheng, X., Li, C., et al., 2022a. Phase transfer of Mo2C induced by boron doping to boost nitrogen reduction reaction catalytic activity. Adv. Funct. Mater. 32, 2110783.
Fan, K., Xie, W., Li, J., Sun, Y., Xu, P., Tang, Y., et al., 2022b. Active hydrogen boosts electrochemical nitrate reduction to ammonia. Nat. Commun. 13, 7958.
Fangkoch, S., Boonkum, S., Ratchahat, S., Koo-Amornpattana, W., Eiad-Ua, A., Kiatkittipong, W., et al., 2020. Solvent-free hydrodeoxygenation of triglycerides to diesel-like hydrocarbons over pt-decorated MoO2 catalysts. ACS Omega 5, 6956–6966.
Gao, L., Li, J., Yang, G., Zhang, J., Xie, Z., 2020. De-ammonification using direct contact membrane distillation – an experimental and simulation study. Sep. Purif. Technol. 250, 117158.
Gao, J., Shi, N., Guo, X., Li, Y., Bi, X., Qi, Y., et al., 2021. Electrochemically selective ammonia extraction from nitrate by coupling electron- and phase-transfer reactions at a three-phase interface. Environ. Sci. Technol. 55, 10684–10694.
Gao, J., Shi, N., Li, Y., Jiang, B., Marhaba, T., Zhang, W., 2022. Electrocatalytic upcycling of nitrate wastewater into an ammonia fertilizer via an electrified membrane. Environ. Sci. Technol. 56, 11602–11613.
Garcia-Segura, S., Lanzarini-Lopes, M., Hristovski, K., Westerhoff, P., 2018. Electrocatalytic reduction of nitrate: fundamentals to full-scale water treatment applications. Appl. Catal. B Environ. 236, 546–568.
Gong, Z., Zhong, W., He, Z., Liu, Q., Chen, H., Zhou, D., et al., 2022. Regulating surface oxygen species on copper (I) oxides via plasma treatment for effective reduction of nitrate to ammonia. Appl. Catal. B Environ. 305, 121021.
He, H., Chen, H., Chen, J., Jia, C., Chen, J., Liang, J., et al., 2022a. Dual sites modulating MoO2 nanospheres for synergistically enhanced electrocatalysis of water oxidation. Chem. Eng. J. 443, 136339.
He, W., Zhang, J., Dieckhofer, S., Varhade, S., Brix, A.C., Lielpetere, A., et al., 2022b. Splicing the active phases of copper/cobalt-based catalysts achieves high-rate tandem electroreduction of nitrate to ammonia. Nat. Commun. 13, 1129.
Kani, N.C., Gauthier, J.A., Prajapati, A., Edgington, J., Bordawekar, I., Shields, W., et al., 2021. Solar-driven electrochemical synthesis of ammonia using nitrate with 11% solar-to-fuel efficiency at ambient conditions. Energy Environ. Sci. 14, 6349–6359.
Li, J., Yang, Q.-Q., Hu, Y.-X., Liu, M.-C., Lu, C., Zhang, H., et al., 2019. Design of lamellar Mo2C nanosheets assembled by Mo2C nanoparticles as an anode material toward excellent sodium-ion capacitors. ACS Sustain. Chem. Eng. 7, 18375–18383.
Li, X., Wang, S., Wang, G., Shen, P., Ma, D., Chu, K., 2022a. Mo2C for electrocatalytic nitrate reduction to ammonia. Dalton Trans. 51, 17547–17552.
Li, Y., Ma, J., Wu, Z., Wang, Z., 2022b. Direct electron transfer coordinated by oxygen vacancies boosts selective nitrate reduction to N2 on a co-CuOx electroactive filter. Environ. Sci. Technol. 56, 8673–8681.
Liu, H., Li, X., Zhang, Z., Nghiem, L., Gao, L., Wang, Q., 2021. Semi-continuous anaerobic digestion of secondary sludge with free ammonia pretreatment: focusing on volatile solids destruction, dewaterability, pathogen removal and its implications. Water Res. 202, 117481.
Meghdadi, A., 2018. Characterizing the capacity of hyporheic sediments to attenuate groundwater nitrate loads by adsorption. Water Res. 140, 364–376.
Picetti, R., Deeney, M., Pastorino, S., Miller, M.R., Shah, A., Leon, D.A., et al., 2022. Nitrate and nitrite contamination in drinking water and cancer risk: a systematic review with meta-analysis. Environ. Res. 210, 112988.
Qin, T., Wang, Z., Wang, Y., Besenbacher, F., Otyepka, M., Dong, M., 2021. Recent progress in emerging two-dimensional transition metal carbides. Nano-micro Lett. 13, 183.
Qin, J., Wu, K., Chen, L., Wang, X., Zhao, Q., Liu, B., et al., 2022. Achieving high selectivity for nitrate electrochemical reduction to ammonia over MOF-supported RuxOy clusters. J. Mater. Chem. A 10, 3963–3969.
Ren, X., Zhao, J., Wei, Q., Ma, Y., Guo, H., Liu, Q., et al., 2019. High-performance N2-to-NH3 conversion electrocatalyzed by Mo2C nanorod. ACS Cent. Sci. 5, 116–121.
Sun, J., Garg, S., Xie, J., Zhang, C., Waite, T.D., 2022. Electrochemical reduction of nitrate with simultaneous ammonia recovery using a flow cathode reactor. Environ. Sci. Technol. 56, 17298–17309.
Teng, M., Ye, J., Wan, C., He, G., Chen, H., 2022. Research progress on cu-based catalysts for electrochemical nitrate reduction reaction to ammonia. Ind. Eng. Chem. Res. 61, 14731–14746.
Wan, J., Wu, J., Gao, X., Li, T., Hu, Z., Yu, H., et al., 2017. Structure confined porous Mo2C for efficient hydrogen evolution. Adv. Funct. Mater. 27, 1703933.
Wang, Q., Sun, J., Liu, S., Gao, L., Zhou, X., Wang, D., Song, K., Nghiem, L., 2019. Free ammonia pretreatment improves anaerobic methane generation from algae. Water Res. 162, 269–275.
Wang, Y., Xu, A., Wang, Z., Huang, L., Li, J., Li, F., et al., 2020a. Enhanced nitrate-to-ammonia activity on copper-nickel alloys via tuning of intermediate adsorption. J. Am. Chem. Soc. 142, 5702–5708.
Wang, Y., Zhang, Z., Mao, Y., Wang, X., 2020b. Two-dimensional nonlayered materials for electrocatalysis. Energy Environ. Sci. 13, 3993–4016.
Wang, J., Cai, C., Wang, Y., Yang, X., Wu, D., Zhu, Y., et al., 2021. Electrocatalytic reduction of nitrate to ammonia on low-cost ultrathin CoOx nanosheets. ACS Catal. 11, 15135–15140.
Wang, Y., Li, H., Zhou, W., Zhang, X., Zhang, B., Yu, Y., 2022. Structurally disordered RuO2 nanosheets with rich oxygen vacancies for enhanced nitrate electroreduction to ammonia. Angew. Chem. Int. Ed. 61, 202202604.
Xu, H., Lin, C., Shen, Z., Gao, L., Lin, T., Tao, H., Chen, W., Luo, J., Lu, C., 2020. Molecular characteristics of dissolved organic nitrogen and its interaction with microbial communities in a prechlorinated raw water distribution system. Environ. Sci. Technol. 54 (3), 1484–1492.
Xu, H., Chen, J., Zhang, Z., Hung, C.T., Yang, J., Li, W., 2022a. In situ confinement of ultrasmall metal nanoparticles in short mesochannels for durable electrocatalytic nitrate reduction with high efficiency and selectivity. Adv. Mater. 35, 2207522.
Xu, H., Ma, Y., Chen, J., Zhang, W.X., Yang, J., 2022b. Electrocatalytic reduction of nitrate - a step towards a sustainable nitrogen cycle. Chem. Soc. Rev. 51, 2710–2758.
Yang, L., Xu, H., He, C., Shen, Z., Chen, W., Gao, L., Lin, C., Lin, T., Lu, C., Shi, Q., Luo, J., Wang, W., 2019. Transformation and fate of dissolved organic nitrogen in drinking water supply system: a full scale case study from Yixing, China. Sci. Total Environ. 673, 435–444.
Yin, H., Chen, Z., Xiong, S., Chen, J., Wang, C., Wang, R., et al., 2021. Alloying effect-induced electron polarization drives nitrate electroreduction to ammonia. Chem. Cataly. 1, 1088–1103.
Zhang, K., Zhang, G., Qu, J., Liu, H., 2018. Tungsten-assisted phase tuning of molybdenum carbide for efficient electrocatalytic hydrogen evolution. ACS Appl. Mater. Interfaces 10, 2451–2459.
Zhang, G., Ji, Q., Zhang, K., Chen, Y., Li, Z., Liu, H., et al., 2019. Triggering surface oxygen vacancies on atomic layered molybdenum dioxide for a low energy consumption path toward nitrogen fixation. Nano Energy 59, 10–16.
Zhang, Z., Li, X., Liu, H., Gao, L., Wang, Q., 2021. Free ammonia pretreatment enhances the removal of antibiotic resistance genes in anaerobic sludge digestion. Chemosphere 279, 130910.
Zhang, H., Li, H., Ma, M., Ma, B., Liu, H., Niu, L., et al., 2022a. Nitrogen reduction by aerobic denitrifying fungi isolated from reservoirs using biodegradation materials for electron donor: capability and adaptabilityin the lower C/N raw water treatment. Sci. Total Environ. 864, 161064.
Zhang, N., Shang, J., Deng, X., Cai, L., Long, R., Xiong, Y., et al., 2022b. Governing interlayer strain in bismuth nanocrystals for efficient ammonia electrosynthesis from nitrate reduction. ACS Nano 16, 4795–4804.
Zhao, Q., Chen, S., Ren, H., Chen, C., Yang, W., 2021. Ruthenium nanoparticles confined in covalent organic framework/reduced graphene oxide as wlectrocatalyst toward hydrogen evolution reaction in alkaline media. Ind. Eng. Chem. Res. 60, 11070–11078.
Zheng, W., Zhu, L., Yan, Z., Lin, Z., Lei, Z., Zhang, Y., et al., 2021. Self-activated ni cathode for electrocatalytic nitrate reduction to ammonia: from fundamentals to scale-up for treatment of industrial wastewater. Environ. Sci. Technol. 55, 13231–13243.
Zhong, Y., Xia, X., Shi, F., Zhan, J., Tu, J., Fan, H.J., 2016. Transition metal carbides and nitrides in energy storage and conversion. Adv. Sci. (Weinh) 3, 1500286.